

Use of thermal sieve to allow optical testing of cryogenic optical systems

Dae Wook Kim,* Wenrui Cai, and James H. Burge

College of Optical Sciences, University of Arizona, 1630 E. University Blvd, Tucson, Arizona 85721, USA
*letter2dwwk@hotmail.com

Abstract: Full aperture testing of large cryogenic optical systems has been impractical due to the difficulty of operating a large collimator at cryogenic temperatures. The Thermal Sieve solves this problem by acting as a thermal barrier between an ambient temperature collimator and the cryogenic system under test. The Thermal Sieve uses a set of thermally controlled baffles with array of holes that are lined up to pass the light from the collimator without degrading the wavefront, while attenuating the thermal background by nearly 4 orders of magnitude. This paper provides the theory behind the Thermal Sieve system, evaluates the optimization for its optical and thermal performance, and presents the design and analysis for a specific system.

©2012 Optical Society of America

OCIS codes: (220.4840.) Testing; (120.3940) Metrology.

References and links

1. M. Clampin, "Status of the James Webb Space Telescope (JWST)," Proc. SPIE **7010**, 70100L, 70100L-7 (2008).
2. D. M. Chaney, J. B. Hadaway, J. Lewis, B. Gallagher, and B. Brown, "Cryogenic performance of the JWST primary mirror segment engineering development unit," Proc. SPIE **8150**, 815008, 815008-12 (2011).
3. S. C. West, S. H. Bailey, J. H. Burge, B. Cuerden, J. Hagen, H. M. Martin, and M. T. Tuell, "Wavefront control of the Large Optics Test and Integration Site (LOTIS) 6.5m collimator," Appl. Opt. **49**(18), 3522–3537 (2010).
4. D. W. Kim and J. H. Burge, "cryogenic thermal mask for space-cold optical testing for space optical systems," in OF&T, OSA Technical Digest Series (Optical Society of America), FTuS2 (2010).
5. S. B. Hutchison, A. Cochrane, S. McCord, and R. Bell, "Update status and capabilities for the LOTIS 6.5 meter collimator," Proc. SPIE **7106**, 710618, 710618-12 (2008).
6. E. Hecht, *Optics*, 4th ed. (Pearson Education, 2002), Chap. 10.
7. J. Goodman, *Introduction to Fourier Optics*, 3rd ed. (Roberts & Company Publishers, 2005), Chap. 4.

1. Introduction

The aperture sizes of space optical systems have been increased to achieve higher resolution and more light collecting capability. For instance, James Webb Space Telescope (JWST) has a 6.5m primary mirror aperture diameter [1]. Since space optical systems are very difficult (or impossible) to be repaired while they are operating in space, the final performance test in a space-like environment is essential for a successful space optical system development.

For a space optical system, the whole system is tested inside a cryogenic vacuum chamber which simulates the actual operating environment. With the controlled environment, the optical system can be verified for its optical performance while operating in space. For an example, the JWST primary mirror, which is designed to observe the infrared light from distant stars and galaxies, has to be kept about 25-40K [1, 2].

Common test configurations have a collimator in a cryogenic vacuum chamber to provide a collimated test beam. The test beam passes through the optical system under test and is measured to evaluate the system performance.

For the cryogenic thermal control inside the vacuum chamber, the heat transfer to the optical system under test needs to be minimized. Any unwanted heat transfer may cause thermal gradient over the optical system which causes optical performance degradation of the system. There are three types of heat transfer processes that need to be considered. i) Convection: There is almost no thermal transfer through the convection process inside high vacuum due to the absence of air. ii) Conduction: The optical system needs to be isolated (*i.e.*

no direct contact) from any heat sources. iii) Radiation: Thermal radiation from a hot object needs to be blocked before it reaches to the optical system.

Because the collimator inside the vacuum chamber directly faces the optical system, the thermal radiation from the collimator becomes a critical issue for the cryogenic thermal control. One obvious solution may be a collimator operating at the same temperature as the space optical system, so that they are at a thermal equilibrium. However, making such a customized cryogenic collimator working at a particular cryogenic (*e.g.* ~35K) temperature may cost a significant portion of the total project budget. Thus, it is highly desired to use an existing collimator such as LOTIS operating at an ambient temperature (*e.g.* ~300K) [3].

A new optical testing configuration utilizing Thermal Sieve (TS), a.k.a. cryogenic thermal mask, was developed and introduced [4]. It provides effective thermal decoupling between a cryogenic optical system under test and a collimator operating at an ambient temperature, while passing the test beam without significant degradation in its wavefront. The overall concept of the TS is given in Section 2. Some practical design issues for the TS are discussed in Section 3. Thermal and optical performance of the TS is evaluated in Section 4. The summary and future works are stated in Section 5.

2. Cryogenic optical testing using Thermal Sieve

2.1 Optical testing configuration using TS

A Thermal Sieve consists of consecutive thermal plates, which have an aligned array of holes as shown in Fig. 1 (left). The holes are lined up, so the geometric propagation of a collimated beam (black rays) will pass. The light will be impeded only by the fraction of the area subtended by the holes. (Diffraction effects make this more complicated as discussed in Section 3.) The thermal radiation (red rays), which is diffuse by definition, is not passed efficiently by the collimated holes.

These thermal plates are placed between the collimator and the optical system under test as shown in Fig. 1 (right). There are four major design parameters for a TS; i) N : Number of thermal plates, ii) S : Spacing between the thermal plates, iii) D_{hole} : hole diameter, and iv) I : Interval between holes.

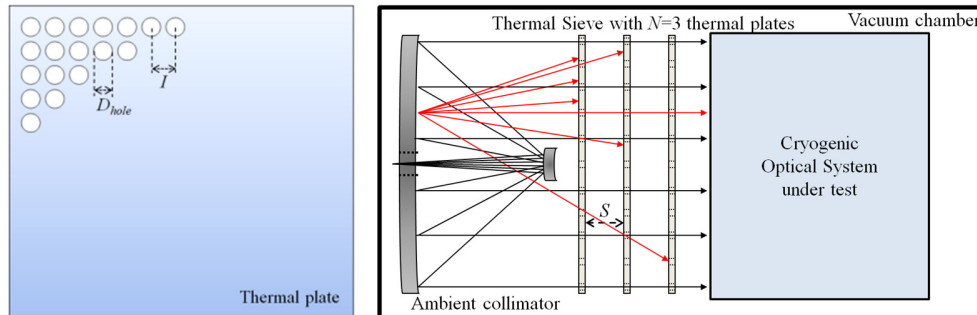


Fig. 1. Thermal plate with array of holes (left) and a conceptual cryogenic optical testing configuration using TS in a vacuum chamber (right) (Note: The red rays represent the thermal radiation from the collimator, and the black rays represent the collimated test beam.).

A point source projected to infinity by the large collimator provides a collimated test beam (black rays in Fig. 1 (right)). This collimated beam passes through the array of holes in the TS. Because of the diffraction from the array of holes, the test beam has multiple diffraction orders. (Analytical wave propagation calculations are presented in Section 3.2.) Those orders represent multiple plane waves with different propagation angles, and the plane waves are fed in to the optical system under test.

The optical system under test maps the angular spectrum (*i.e.* propagation angle) of the test beam to a spatial light distribution at the focal plane. Different diffraction orders at the focal plane represent the Point Spread Function (PSF) of the system for different field angles.

By evaluating the zero order (*i.e.* on-axis) PSF only, various optical testings (*e.g.* wavefront measurement, point source imaging) can be made downstream [5].

2.2 Thermal transfer control using TS

The main function of a Thermal Sieve is control of thermal transfer. The thermal transfer between the plates is limited by the emissivity of the plates and the relatively small area encompassed by the holes. This is conceptually depicted in Fig. 1 (right) as red rays, which represent the thermal radiation from the ambient collimator. The temperature of each thermal plate is independently controlled to gradually match the temperature difference between the collimator and the optical system spaces.

For a simplified thermal transfer model, the propagation of thermal energy via the transmission through the holes and the radiation from the plates needs to be considered. The thermal transfer from an ambient collimator to a cryogenic optical system was modeled with number of graybodies in the vacuum chamber as shown in Fig. 2.

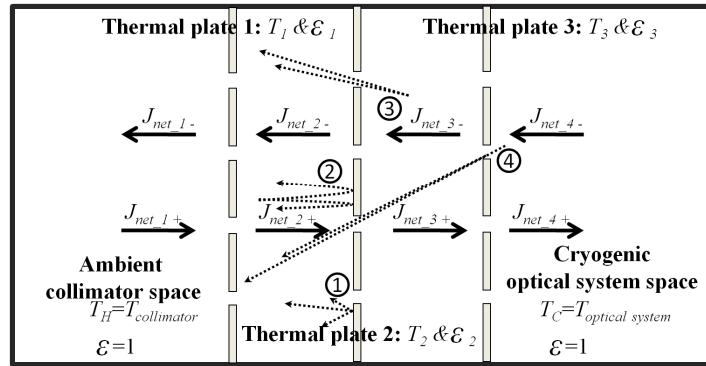


Fig. 2. Schematic thermal transfer model with three thermal plates in a vacuum chamber. The solid arrows represent the net emissive power in each space. Also, as an example, four emissive power components contributing to $J_{net,2-}$ are depicted as dotted arrows 1-4. (1) Graybody radiation from the 2nd thermal plate, (2) Reflection of $J_{net,2+}$ by the 2nd thermal plate, (3) Leak of $J_{net,3-}$ through the 2nd plate holes except the power directly passes through the 1st plate holes, and (4) Leak of $J_{net,4-}$ through the 3rd and 2nd plate holes except the power directly passes through the 1st plate holes.

The collimator and optical system spaces were represented by two blackbodies with their operating temperatures T_H and T_C . (For more accurate calculations, these spaces may be modeled including the actual collimator and optical system with reflecting and radiating surfaces.) As an example configuration, three thermal plates were set as graybodies with controlled temperatures $T_{1,3}$ and emissivity $\epsilon_{1,3}$ values. The emissive power J from these graybodies is given from Stefan-Boltzmann law

$$J = \epsilon \cdot \sigma \cdot T^4 \quad [W / m^2] \quad (1)$$

where ϵ is the emissivity, σ is the Stefan-Boltzmann constant $5.67 \times 10^{-8} \text{ W/m}^2/\text{K}^4$, and T is the absolute temperature of the graybody.

Considering the thermal equilibrium in each space between two thermal plates, a set of thermal transfer equations is determined. For instance, the net emissive power $J_{net,2-}$ should be equal to the sum of the four emissive power components depicted as dotted arrows in Fig. 2. Then, the thermal transfer equation becomes

$$\begin{aligned}
J_{net_2-} &= \varepsilon_2 \cdot \sigma \cdot T_2^4 \cdot \alpha && : (1) \text{ in Fig. 2.} \\
&+ J_{net_2+} \cdot (1 - \varepsilon_2) \cdot \alpha && : (2) \text{ in Fig. 2.} \\
&+ J_{net_3-} \cdot \frac{(\pi - \Omega_{eff1})}{\pi} \cdot (1 - \alpha) && : (3) \text{ in Fig. 2.} \\
&+ J_{net_4-} \cdot \frac{(\Omega_{eff1} - \Omega_{eff2})}{\pi} \cdot (1 - \alpha) && : (4) \text{ in Fig. 2.}
\end{aligned} \tag{2}$$

where the obscuration ratio α of each thermal plate was defined as the ratio of the not-a-hole region area to the whole thermal plate area. Two effective solid angle Ω_{eff1} and Ω_{eff2} represent the sum of solid angles encompassed by the array of holes in the neighboring plate (S away) and the following plate ($2S$ away), respectively. These solid angles are expressed using approximated projected solid angles with $\cos^4\theta$ scale factor as

$$\Omega_{eff1} \cong \frac{\pi \cdot (D_{hole}/2)^2}{S^2} \left(1 + 4 \sum_{n=1}^{\infty} \cos^4 \theta\right) = \frac{\pi \cdot D_{hole}^2}{4S^2} \left\{1 + 4 \sum_{n=1}^{\infty} \left(\frac{S}{\sqrt{S^2 + I^2(n^2 + m^2)}}\right)^4\right\} \tag{3}$$

and

$$\Omega_{eff2} \cong \frac{\pi \cdot (D_{hole}/2)^2}{(2S)^2} \left(1 + 4 \sum_{n=1}^{\infty} \cos^4 \theta\right) = \frac{\pi \cdot D_{hole}^2}{16S^2} \left\{1 + 4 \sum_{n=1}^{\infty} \left(\frac{S}{\sqrt{S^2 + I^2(n^2 + m^2)}}\right)^4\right\} \tag{4}$$

where θ is the angle shown in Fig. 3. The n and m represent the relative column and row differences between two holes in the thermal plates as depicted in Fig. 3. Infinite number of holes (i.e. infinite n and m) was assumed instead of using the actual number of the holes. This eliminates the geometrical asymmetry problem (e.g. edge effect) for evaluating the effective solid angles not at the center of thermal plate. Fortunately, due to the rapid drop of $\cos^4\theta$, this assumption hardly affects the evaluated solid angle values.

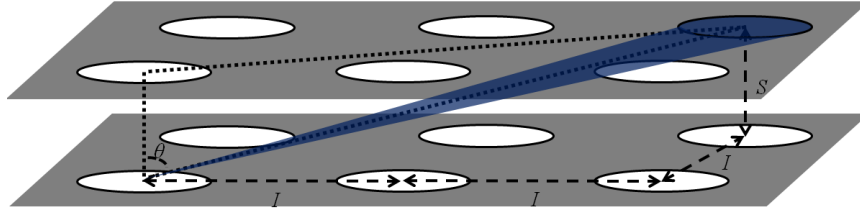


Fig. 3. Projected solid angle geometry between a hole at the bottom thermal plate and another hole at the top plate (S : spacing between the plates, I : interval between holes) for $n = 2$ and $m = 1$ case in Eq. (3).

By solving the set of thermal transfer equations the thermal loads to the optical system space and the collimator space can be evaluated. Those thermal loads can be minimized via optimizing TS design parameters such as thermal plate's temperatures and emissivity values. A detailed thermal performance analysis using a case study focused on the optical system space is given in Section 4.1.

3. Thermal Sieve design considerations

3.1 Independence between hole-sets

The wave propagation going through a large array of hole-sets, where a hole-set represents N holes aligned along the optical axis as the test beam passes through the N thermal plates in Fig. 1 (right), is a numerically demanding simulation due to the interaction among the complex light fields from the thousands of hole-sets. Especially, the periodic pattern needs to

be perturbed to model imperfect alignment, and it becomes almost an impossible simulation task within today's computing power.

This entanglement issue can be ignored if each complex field is almost confined within its own hole-set while it propagates through. This independence assumption allows us to express the complex field right after passing the TS in a simple form as presented in Section 3.2. The tolerance analysis in Section 4.2 is also performed based on this assumption.

In order to accomplish this independence condition, the holes need to be large enough that the light remains mostly collimated in the region between plates. Also, the interval between holes I needs to be larger than the extent of diffraction spread in the geometrical shadow region (*i.e.* outside a hole). Then, most of the light can go straight through a hole-set without interacting with other holes. In other words, the diffraction spread needs to be small compared to the hole size D_{hole} and the interval I between the holes. (Note: $I > D_{hole}$ by definition shown in Fig. 1.) Using the edge diffraction model [6], which approximates the spread from the circular aperture edge, a condition for D_{hole} defined in terms of wavelength λ and propagation distance S as

$$D_{hole} > 2\sqrt{\frac{\lambda \cdot S}{2}} \quad (5)$$

A scale factor of 2 was applied to take account the spread in both directions, and the extent of the spread was chosen where the irradiance drops down to $< \sim 5\%$ of the nominal irradiance from the edge diffraction model [6].

These independence conditions were investigated by performing rigorous wave propagation simulations through an example hole-set using Fresnel diffraction model [7]. TS design parameters in Table 1, which satisfy Eq. (5), were used for the simulation.

Table 1. TS Design Parameter Values for a Hole-set Wave Propagation Simulation

Parameters	Symbol	Value
Diameter of a hole	D_{hole}	0.002 m
Interval between holes	I	0.02 m
Spacing between plates	S	0.25 m
Number of thermal plates	N	3
Wavelength	λ	1 μ m

An electric field in an x-y plane is expressed using complex field notations as

$$U(x, y) = A(x, y) \cdot \exp(i \cdot \frac{2\pi}{\lambda} \cdot \Phi(x, y)) \quad (6)$$

where A is the amplitude, Φ is the phase in waves, λ is the wavelength of the field. The actual field is the real part of this complex field. Based on the Fresnel near-field diffraction model [7] the complex field at the next thermal plate $U_n(x_n, y_n)$ becomes

$$U_n(x_n, y_n) \propto F_{\eta=\frac{y_n}{\lambda \cdot S}} F_{\xi=\frac{x_n}{\lambda \cdot S}} [U_p(x_p, y_p) \cdot \exp\{\frac{i \cdot \pi}{\lambda \cdot S} (x_p^2 + y_p^2)\}] \quad (7)$$

where FF represents the 2D Fourier transform, $U_p(x_p, y_p)$ is the complex field at the previous thermal plate, and S is the distance between thermal plates (*i.e.* propagation distance).

The collimated test beam was propagated through the three holes in a hole-set and evaluated after the last hole in the 3rd thermal plate. The resulting intensity distribution (*i.e.* squared modulus of the complex field) at each holes are presented in Fig. 4.

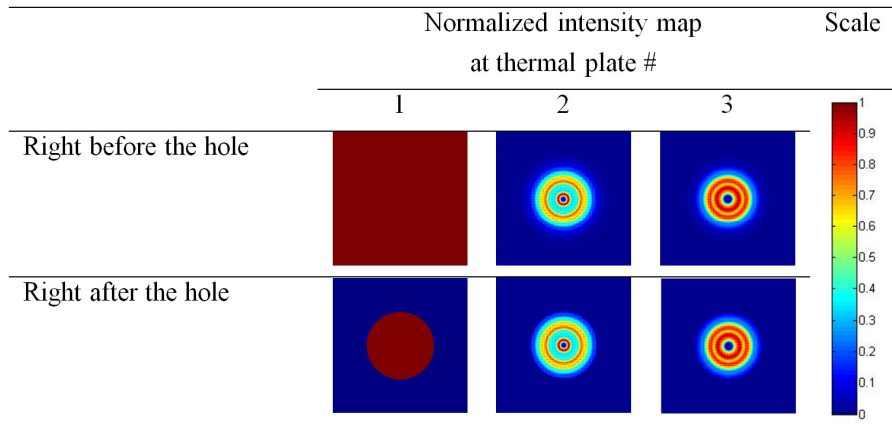


Fig. 4. Normalized intensity distribution of the complex fields at each thermal plate as the test beam passes through a hole-set.

Two profiles of the intensity distributions are presented in Fig. 5. These are the intensity distributions right before the 2nd and 3rd thermal plates. Most of the field intensity is still stays inside the physical hole area, and the intensity rapidly decreases beyond the geometrical shadow boundary. As predicted in Eq. (5), the diffraction spread is $< \sim 0.7\text{mm}$.

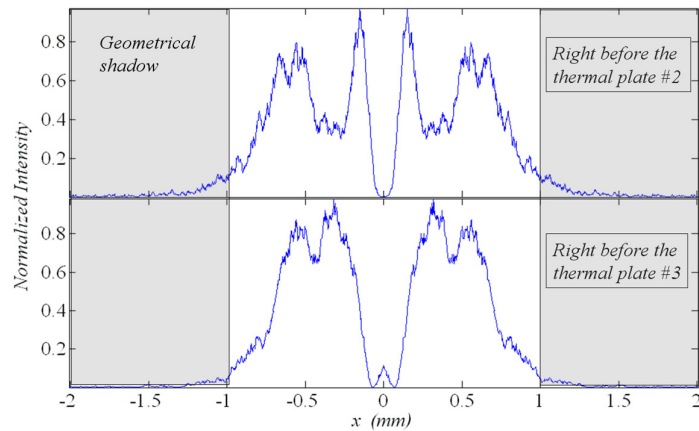


Fig. 5. x-profiles of the normalized intensity distribution of the test beam right before the 2nd and 3rd hole in the thermal plates (The shaded region represents the geometrical shadow region.).

Thus, the spatial extend of the test beam passing through the hole-set, which satisfies the independence conditions in Eq. (5), is almost confined within its own hole-set without interacting with other hole-sets.

3.2 Separation of multiple diffraction orders

The multiple diffraction orders from the array of holes need to be spatially separated for the zero order selection mentioned in Section 2.1. The optical system under test was simplified as an ideal imaging system with an effective focal length f_{eff} for this discussion. This is a valid approximation since the location of different diffraction orders depends only on the focal length f_{eff} . (Of course, the specific shape of the complex field still depends on the physical properties of the actual system such as aperture shape and size.)

For the wave propagation to the focal plane of the optical system under test, the Fraunhofer far-field diffraction theory was used [7]. The complex field at the focal plane of

the optical system U_{focal} is expressed in a 2D Fourier transform of the test beam complex field U_{TS} as

$$U_{focal}(x, y) \propto F_{\eta=\frac{y}{\lambda \cdot f_{eff}}} F_{\xi=\frac{x}{\lambda \cdot f_{eff}}} [U_{TS}(x, y)] \quad (8)$$

where f_{eff} is the effective focal length of the optical system under test. The complex field U_{TS} is the complex field after passing through the TS, and can be expressed as

$$U_{TS}(x, y) = cyl\left(\frac{\sqrt{x^2 + y^2}}{D_{TS}}\right) \cdot \left\{ comb\left(\frac{x}{I}, \frac{y}{I}\right) ** U_{hole}(x, y) \right\} \quad (9)$$

where ** represents the 2D convolution, I is the interval between holes, D_{TS} is the diameter of the TS circular aperture, and U_{hole} is the complex field in a hole at the last thermal plate. Identical complex field U_{hole} was assumed for all holes at the last thermal plate thanks to the independence assumption in Section 3.1, so that U_{TS} was expressed using 2D *comb* function defined in Appendix A.1.

By inserting Eq. (9) to Eq. (8), the complex field at the focal plane becomes

$$\begin{aligned} U_{focal}(x, y) &\propto F_{\eta=\frac{y}{\lambda \cdot f_{eff}}} F_{\xi=\frac{x}{\lambda \cdot f_{eff}}} \left[cyl\left(\frac{\sqrt{x^2 + y^2}}{D_{TS}}\right) \cdot \left\{ comb\left(\frac{x}{I}, \frac{y}{I}\right) ** U_{hole}(x, y) \right\} \right] \\ &= F_{\eta=\frac{y}{\lambda \cdot f_{eff}}} F_{\xi=\frac{x}{\lambda \cdot f_{eff}}} \left[cyl\left(\frac{\sqrt{x^2 + y^2}}{D_{TS}}\right) \right] ** F_{\eta=\frac{y}{\lambda \cdot f_{eff}}} F_{\xi=\frac{x}{\lambda \cdot f_{eff}}} \left[comb\left(\frac{x}{I}, \frac{y}{I}\right) ** U_{hole}(x, y) \right] \quad (10) \\ &\propto somb\left(\frac{D_{TS} \cdot \sqrt{x^2 + y^2}}{\lambda \cdot f_{eff}}\right) ** \left\{ comb\left(\frac{I \cdot x}{\lambda \cdot f_{eff}}, \frac{I \cdot y}{\lambda \cdot f_{eff}}\right) \cdot F_{\eta=\frac{y}{\lambda \cdot f_{eff}}} F_{\xi=\frac{x}{\lambda \cdot f_{eff}}} [U_{hole}(x, y)] \right\} \end{aligned}$$

which is a convolution of the sombrero function *somb* (defined in Appendix A.1) and the modulated *comb* function. The intensity distribution Q of the *somb* function is the well-known Airy disk pattern in Eq. (11).

$$Q_{focal_somb}(x, y) \propto \left| U_{focal_somb}(x, y) \right|^2 = \left| somb\left(\frac{D_{TS} \cdot \sqrt{x^2 + y^2}}{\lambda \cdot f_{eff}}\right) \right|^2 \quad (11)$$

The Airy disk diameter D_{Airy} is defined as the diameter of the first minimum intensity circle as

$$D_{Airy} \approx \frac{2.44 \cdot \lambda \cdot f_{eff}}{D_{TS}} \quad (12)$$

and shown in Fig. 6 (left). Another part of U_{focal} in Eq. (10) is the modulated *comb* function. The relative amplitude and phase factor for each delta function in the comb function depends on the Fourier transform of U_{hole} . However, the spatial locations of those delta functions are defined simply by the interval K given as

$$K = \frac{\lambda \cdot f_{eff}}{I} \quad (13)$$

for the effective focal length f_{eff} , wavelength λ and the interval between holes I .

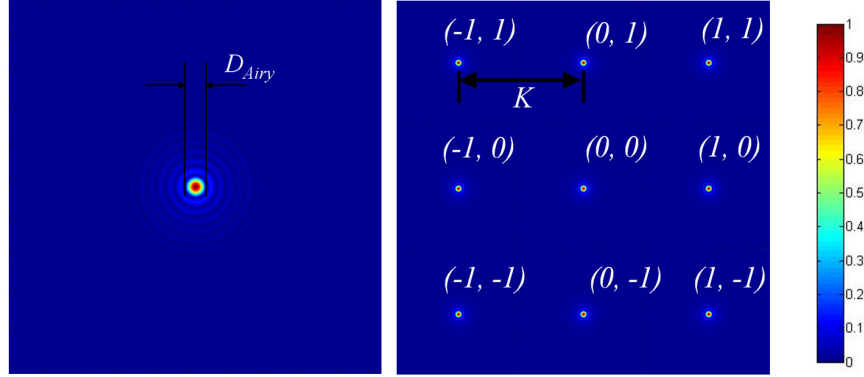


Fig. 6. Normalized Airy disk pattern (left), and the first nine diffraction orders at the focal plane of the optical system under test (right).

The total intensity distribution of U_{focal} in Eq. (10) becomes an array of many Airy disk patterns spaced by K . The first nine diffraction orders from $(-1, -1)$ to $(1, 1)$ order are shown in Fig. 6 (right). These diffraction orders, for a small K , may overlap to each other. However, if K is large enough compared to the size of the Airy disk D_{Airy} , the orders can be separated from each other without overlapping. Also, for a typical testing configuration, the limiting aperture may be the optical system under test, not the TS. It means that the Airy disk size in Eq. (12) will depend on the diameter of the optical system aperture D_{system} instead of D_{TS} .

Then, the Airy disk size needs to be much smaller than the distance between orders as

$$D_{Airy} \approx \frac{2.44 \cdot \lambda \cdot f_{eff}}{D_{system}} \ll \frac{\lambda \cdot f_{eff}}{I} = K \quad (14)$$

for a given wavelength λ , effective focal length f_{eff} , and the system aperture diameter D_{system} . By re-writing Eq. (14) the interval I between holes needs to satisfy

$$I \ll \frac{D_{system}}{2.44} \quad (15)$$

as a condition for the diffraction order separation.

4. Thermal Sieve performance demonstration

4.1 Thermal performance of TS

The thermal performance of a nominal TS (design parameters in Table 2) was evaluated as a case study. The thermal load to a 35K cold space optical system space from a 300K collimator space was calculated and studied for various situations.

Table 2. Nominal TS Design Parameters

Parameters	Symbol	Value	Etc.
Temperature of hot space	T_H	300 K	LOTIS [3]
Temperature of cold space	T_C	35 K	JWST [1, 2]
Test beam wavelength	λ	1 μm	from Table 1
Diameter of hole	D_{hole}	0.002 m	from Table 1
Interval between holes	I	0.02 m	from Table 1
Spacing between plates	S	0.25 m	from Table 1
Number of thermal plates	N	3	from Table 1
Diameter of optical system	D_{system}	6.5 m	JWST [1]
Number of hole-sets	$N_{hole-set}$	~85500	
Obscuration ratio	A	~0.99	

A set of thermal transfer equations for the TS with three thermal plates was driven from the thermal model in Section 2.2, and expressed in a matrix form as

$$\begin{bmatrix} 1 & 0 & 0 & 0 & 0 & 0 & 0 & 0 \\ (\varepsilon_1 - 1)\alpha & 1 & 0 & (\alpha - 1) & 0 & \Omega_{eff1}(\alpha - 1)/\pi & 0 & \Omega_{eff2}(\alpha - 1)/\pi \\ (\pi - \Omega_{eff1})(\alpha - 1)/\pi & 0 & 1 & (\varepsilon_1 - 1)\alpha & 0 & 0 & 0 & 0 \\ 0 & 0 & (\varepsilon_2 - 1)\alpha & 1 & 0 & (\pi - \Omega_{eff1})(\alpha - 1)/\pi & 0 & (\Omega_{eff1} - \Omega_{eff2})(\alpha - 1)/\pi \\ (\Omega_{eff1} - \Omega_{eff2})(\alpha - 1)/\pi & 0 & (\pi - \Omega_{eff1})(\alpha - 1)/\pi & 0 & 1 & (\varepsilon_2 - 1)\alpha & 0 & 0 \\ 0 & 0 & 0 & 0 & (\varepsilon_3 - 1)\alpha & 1 & 0 & (\pi - \Omega_{eff1})(\alpha - 1)/\pi \\ \Omega_{eff2}(\alpha - 1)/\pi & 0 & \Omega_{eff1}(\alpha - 1)/\pi & 0 & (\alpha - 1) & 0 & 1 & (\varepsilon_3 - 1)\alpha \\ 0 & 0 & 0 & 0 & 0 & 0 & 0 & 1 \end{bmatrix} \begin{bmatrix} J_{net_1+} \\ J_{net_1-} \\ J_{net_2+} \\ J_{net_2-} \\ J_{net_3+} \\ J_{net_3-} \\ J_{net_4+} \\ J_{net_4-} \end{bmatrix} = \begin{bmatrix} \sigma T_H^4 \\ \sigma \varepsilon_1 T_1^4 \alpha \\ \sigma \varepsilon_1 T_1^4 \alpha \\ \sigma \varepsilon_2 T_2^4 \alpha \\ \sigma \varepsilon_2 T_2^4 \alpha \\ \sigma \varepsilon_3 T_3^4 \alpha \\ \sigma \varepsilon_3 T_3^4 \alpha \\ \sigma T_C^4 \end{bmatrix} \quad (16)$$

in terms of the given emissivity values ε_{1-3} , absolute temperature of the thermal plates T_{1-3} , temperature of the hot collimator space T_H , temperature of the cold optical system space T_C , and the obscuration ratio of the thermal plate α . The effective solid angle Ω_{eff1} and Ω_{eff2} were given in Eq. (3) and (4).

By solving Eq. (16) using an inverse matrix calculation, the net emissive power J values are determined. The thermal loads to the optical system space ΔJ_C and the collimator space ΔJ_H are given as

$$\Delta J_C = J_{net_4+} - J_{net_4-} \quad (17)$$

$$\Delta J_H = J_{net_1-} - J_{net_1+} \quad (18)$$

where $J_{net_l \pm}$ and $J_{net_4 \pm}$ are depicted in Fig. 2. A positive thermal load means incoming thermal energy to the space, and a negative value means outgoing thermal energy from the space. The magnitude of these thermal loads needs to be minimized, so that thermal gradients on the optical systems are minimized during the cryogenic testing.

As verification for the analytical thermal transfer equation in Eq. (16), an independent numerical simulation using non-sequential ray tracing was performed on Zemax. The Zemax model was configured in a way that each surface emits, absorbs, reflects, or scatters rays according to the appropriate temperature and emissivity.

In comparison, the thermal loads to the cold optical system space ΔJ_C were plotted as a function of the spacing S between thermal plates. The Zemax simulation results were shown in blue dots and the analytical calculations using Eq. (16) were plotted in red curve. They match well with each other except for very small S values, where the solid angle approximation in Eq. (3) and (4) is no longer valid as the spacing S approaches zero. Since the approximated solid angle is larger than the exact value (e.g. The approximated solid angle goes to infinity as S approaches zero.), Zemax simulation shows less thermal loads for the small spacing values $S < \sim 0.005\text{m}$ in Fig. 7. However, this discrepancy only happens for very small S values, which is impractical to be manufactured anyway.

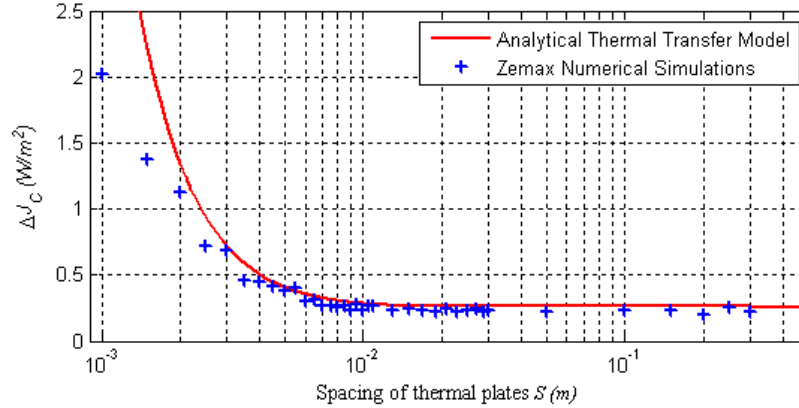


Fig. 7. Comparison between the analytical thermal transfer model in Eq. (16) and the Zemax numerical simulation using non-sequential ray tracing (for $T_1 = 300K$, $T_2 = 252K$, $T_3 = 35K$ and $\varepsilon_1 = \varepsilon_3 = 0.9$, $\varepsilon_2 = 0.1$ case).

As the first thermal performance study, the emissivity values of the thermal plates were varied. The plate's temperature T_1 and T_3 were fixed at the same temperatures as the collimator space temperature and the optical system space temperature, respectively. The second plate's temperature T_2 was varied from 150K to 300K.

The thermal loads ΔJ_C and ΔJ_H for nine different emissivity combinations were calculated and plotted in Fig. 8. For the 1st and 3rd plate, the higher emissivity values showed better thermal performance. In other words, more blackbody-like plate makes the thermal loads closer to 0. The 2nd plate's emissivity ε_2 turned out to be an effective parameter to reduce the thermal loads. For instance, by decreasing ε_2 from 0.15 to 0.05, the thermal loads ΔJ_C (at $T_2 = \sim 280K$) quickly decreases from $\sim 0.6W/m^2$ to $\sim 0.2W/m^2$.

The second plate's temperature T_2 also affects the thermal performance. As shown in Fig. 8 (left), higher T_2 puts more thermal load to the optical system space. In contrast, for the collimator space, higher T_2 makes ΔJ_H closer to 0 in Fig. 8 (right). This becomes a balance problem between ΔJ_C and ΔJ_H . As an example, if the maximum allowable magnitude of the thermal load is $0.3W/m^2$ for both ΔJ_C and ΔJ_H (for $\varepsilon_1 = \varepsilon_3 = 0.9$ and $\varepsilon_2 = 0.1$ case), T_2 may be chosen to be 252K (green long dashed lines in Fig. 8).

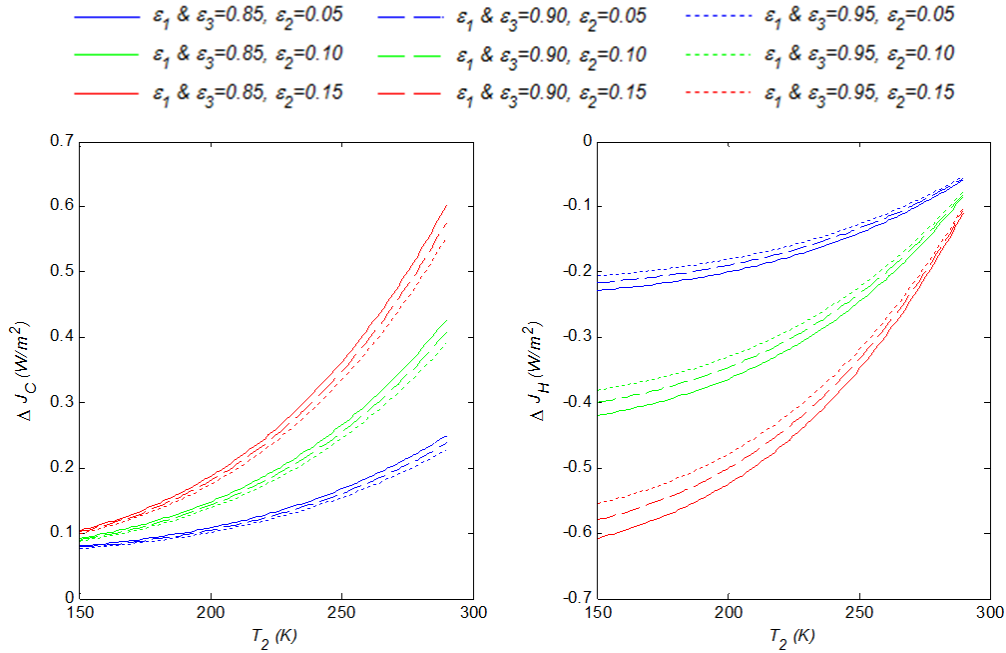


Fig. 8. Thermal loads as a function of the 2nd thermal plate's temperature T_2 for various emissivity values of the thermal plates (Note: $T_1 = 300K$ and $T_3 = 35K$ case).

While fixing T_2 at 252K, the effects of the other two plate's temperatures T_1 and T_3 were investigated. While watching the thermal load change in the optical system space, T_3 was varied from 15K to 45K as shown in Fig. 9 (left). The thermal load ΔJ_C was decreased as the 3rd plate got colder. The effect of T_1 on ΔJ_C was small. The 1st plate's temperature T_1 was changed from 299.9K to 300.1K to look at the effects on the collimator space ΔJ_H . As shown in Fig. 9 (right), the magnitude of ΔJ_H can be minimized (e.g. $0W/m^2$) by setting T_1 at an optimal temperature. The temperature of the 3rd plate T_3 hardly affects ΔJ_H . (All three plots are overlapped in Fig. 9 (right).) In summary, once the emissivity values and T_2 are fixed, T_1 and T_3 may provide a good means to tweak the final thermal performance of a TS.

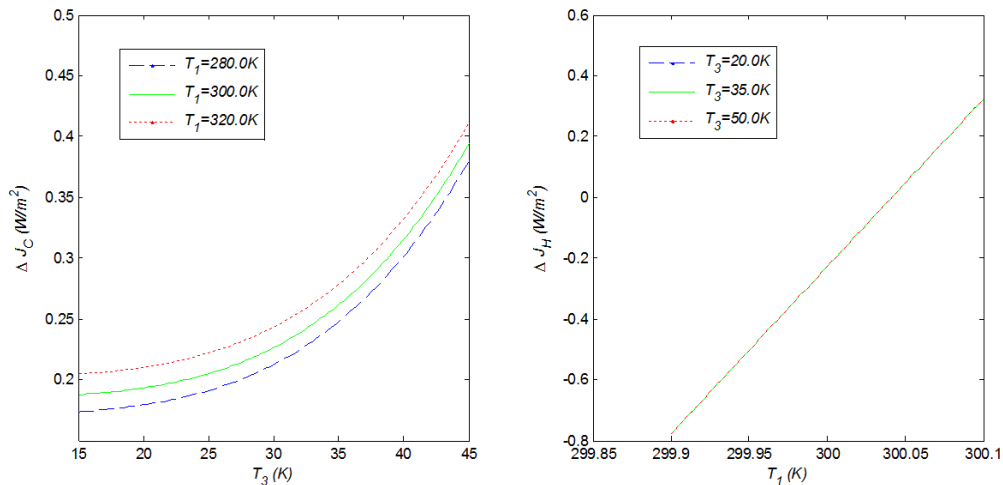


Fig. 9. Thermal analysis of system with T_2 fixed at 252K: Thermal loads to the cold optical system space ΔJ_C (left) and the hot collimator space ΔJ_H (right) (Note: $\epsilon_1 = \epsilon_3 = 0.9$, $\epsilon_2 = 0.1$).

Another interesting idea was studied. Instead of fixing T_2 at a certain temperature, the temperature of the 2nd plate was set to be float. In other words, the 2nd plate was not thermally controlled. The equilibrium temperature T_2 was determined based on the thermal emissive powers $J_{net_{2\pm}}$ and $J_{net_{3\pm}}$. The condition for the thermal equilibrium is

$$\Delta J_2 = J_{net_{2+}} + J_{net_{3-}} - J_{net_{2-}} - J_{net_{3+}} = 0 \quad (19)$$

where ΔJ_2 is the thermal load on the second plate, and $J_{net_{2-3\pm}}$ are the emissive powers depicted in Fig. 2.

The temperature of the 1st and 3rd plate was varied while T_2 was floating at its equilibrium temperature shown in Fig. 10, and the thermal loads ΔJ_C and ΔJ_H were evaluated (Fig. 11). In comparison with the fixed T_2 case in Fig. 9, the thermal loads ΔJ_C for the floating case showed slightly wider range of thermal loads in Fig. 11 (left). For $T_1 = 320K$ case, ΔJ_C for the floating T_2 case in Fig. 11 (left) got slightly higher than the fixed $T_2 = 252K$ case in Fig. 9 (left), because T_2 at thermal equilibrium was $\sim 269K$ as shown in Fig. 10 (left). For $T_1 = 280K$ case, ΔJ_C for the floating T_2 case in Fig. 11 (left) got slightly smaller than the fixed $T_2 = 252K$ case in Fig. 9 (left), because the equilibrium T_2 was $\sim 236K$ as shown in Fig. 10 (left). For ΔJ_H , there was no significant difference between the floating and fixed T_2 cases because the floating temperature T_2 was changing in the very small range 252.2-252.4K, which is practically same as the fixed $T_2 = 252K$.

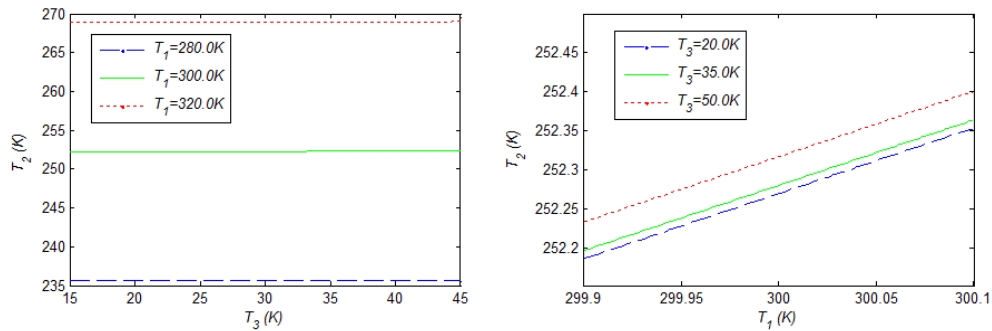


Fig. 10. Thermal equilibrium temperature for the 2nd thermal plate allowed to float: T_2 vs. T_3 (left) and T_1 (right) (Note: $\epsilon_1 = \epsilon_3 = 0.9$, $\epsilon_2 = 0.1$).

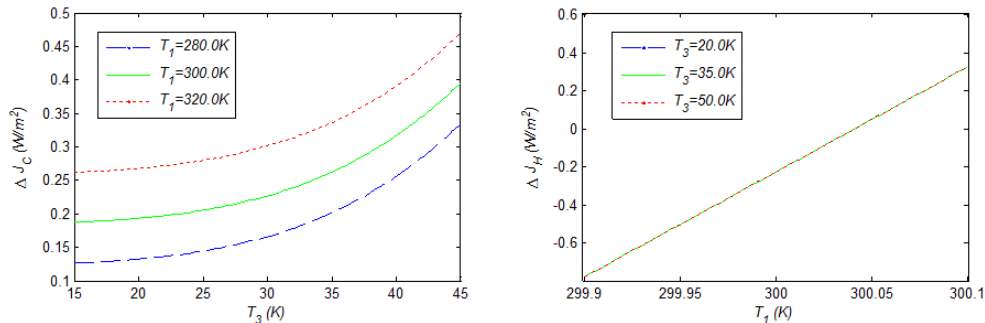


Fig. 11. Thermal analysis of system with T_2 allowed to float: Thermal loads to the cold optical system space ΔJ_C (left) and the hot collimator space ΔJ_H (right) (Note: $\epsilon_1 = \epsilon_3 = 0.9$, $\epsilon_2 = 0.1$).

The benefit of this floating T_2 approach is obvious. The 2nd plate does not need to be thermally controlled. The temperature T_2 is automatically fixed at the equilibrium temperature while the TS gives comparable thermal performance as the fixed T_2 case.

In total, the thermal analysis showed thermal control for isolating a 35K optical system from a 300K collimator. As shown in Fig. 9 and 11, the TS with holes occupying $\sim 1\%$ of the

thermal plate area and with two black (*i.e.* high emissivity) and a polished (*i.e.* low emissivity) thermal plates accomplished thermal loads less than $200\text{mW}/\text{m}^2$ for both the ambient and the cryogenic sides of the testing configuration. This is nearly 4 orders of magnitude attenuation from the 300K collimator's radiating power.

4.2 Optical performance of TS

The test beam in an optical testing configuration with TS goes through the array of holes. A perfectly engineered TS may be fully modeled, simulated and calibrated. However, any actual TS will have variations in mechanical dimensions, which can include each hole's diameter, locations due to misalignment, manufacturing tolerance and thermal deformation. This does not seriously harm the thermal performance of the TS, but does affect the optical performance.

The optical performance of the nominal TS in Table 2 was estimated by performing Monte Carlo simulations based on realistic tolerance values. The test beam was propagated through the holes while the alignment between holes was randomly perturbed within $\pm \delta x$ and $\pm \delta y$. The hole diameter D_{hole} was also varied within $\pm \delta D_{hole}$. One of the simulation results is presented in Fig. 12. The complex field at the last hole of a hole-set is distorted as a result of the misalignment and the hole diameter variation.

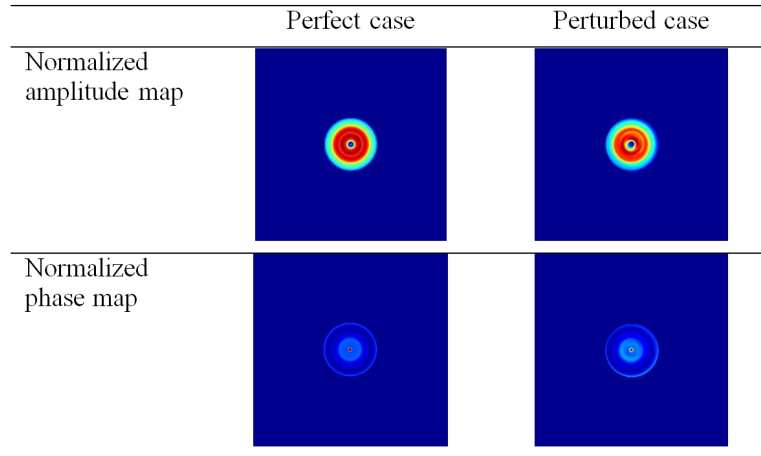


Fig. 12. Comparison between the ideal and distorted complex field at the last hole after the test beam went through a perfect hole-set and a perturbed hole-set, respectively. (Tolerance: $\delta x = 50\mu\text{m}$, $\delta y = 50\mu\text{m}$, and $\delta D_{hole} = 20\mu\text{m}$).

An integrated amplitude error Δ_a and a phase error Δ_p were defined by integrating the complex field over the hole area as expressed in Eq. (20) and (21) to quantitatively assess the optical performance of the perturbed TS compared to the ideal one.

$$\Delta_a = \frac{\left| \iint_{hole} U_{hole_perturbed}(x, y) dx \cdot dy \right| - \left| \iint_{hole} U_{hole_perfect}(x, y) dx \cdot dy \right|}{\left| \iint_{hole} U_{hole_perfect}(x, y) dx \cdot dy \right|} \cdot 100 (\%) \quad (20)$$

$$\Delta_p = \frac{\text{Angle}[\iint_{hole} U_{hole_perturbed}(x, y) dx \cdot dy] - \text{Angle}[\iint_{hole} U_{hole_perfect}(x, y) dx \cdot dy]}{2 \cdot \pi} \quad (\text{waves}) \quad (21)$$

where *Angle* is a function returns the phase angle of a complex field. These definitions simplify the representation and evaluation process of the test beam quality in ~85500 hole-sets.

Variations in amplitude cause intensity fluctuations across the pupil

$$\Delta_i = \frac{\Delta Q}{Q} \cdot 100 \cong 2 \cdot \frac{\Delta A}{A} \cdot 100 = 2 \cdot \Delta_a \quad (22)$$

when small ΔA value is present since the intensity Q is the square of amplitude A . Variations in phase cause wavefront phase to change across the pupil, which degrade the performance of the collimator. The form of the wavefront phase or intensity variation follows the changes in hole size and position. For example, if all the holes are shifted by a same amount, the intensity will be decreased uniformly across the pupil. If holes in a small region are shifted relative to rest of the system, the intensity of the light in that region will be decreases and the wavefront phase in that region will be shifted.

Because of the independence between hole-sets in Section 3.1, the normalized amplitude and phase error for the 85500 hole-sets were individually simulated with given tolerance. The RMS amplitude and phase errors were plotted for various δx , δy , and δD_{hole} tolerance values in Fig. 13.

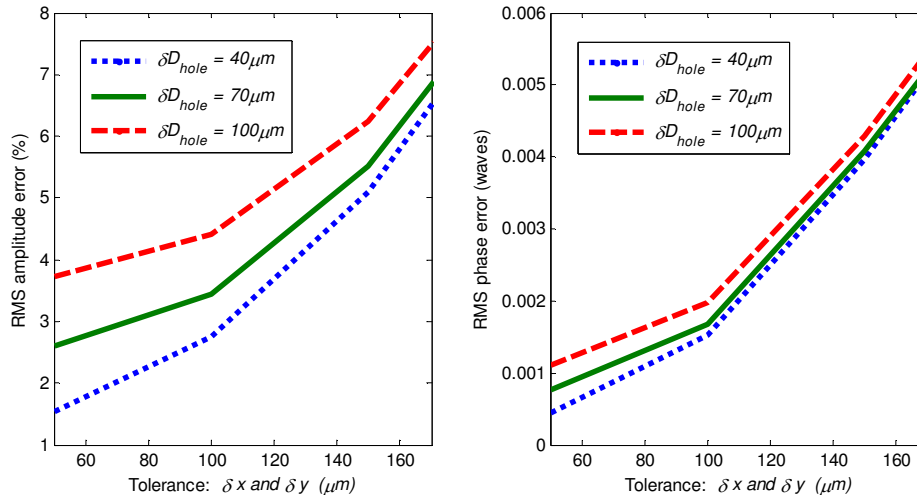


Fig. 13. Variations in the transmitted wavefront amplitude (left) and phase (right) due to variations in hole size and position.

It is clear that larger alignment tolerance, δx and δy , causes more amplitude errors in the test beam as shown in Fig. 13 (left). For $\delta x = \delta y = \delta D_{hole} = 100\mu m$ case, the RMS amplitude error is ~4.2%. If δx and δy are decreased to $50\mu m$, the RMS amplitude error is decreased by ~0.5%. If δD_{hole} is decreased to $70\mu m$, the RMS amplitude error is decreased by ~1%. In other words, the amplitude error is more sensitive to the hole diameter tolerance, which has more direct impact on the energy blocked by the hole. This amplitude error may not be a big issue for most wavefront measurements, which are primarily dependent on the phase of the test beam.

The RMS phase error, shown in Fig. 13 (right), also gets worse as δx , δy and δD_{hole} are increased. While δx and δy varies from $50\mu m$ to $170\mu m$, the RMS phase error increases from ~0.001waves to ~0.005waves. The hole diameter tolerance δD_{hole} also affects the induced RMS phase error, but the impact is relatively small as shown in three different colors in Fig. 13 (right). The alignment tolerance is more important than the hole size tolerance to achieve higher quality test beam phase. The RMS phase error were <0.006waves RMS for all the

tolerance ranges investigated in this section, which seems promising for most optical testing applications.

5. Concluding remarks

A new conceptual testing configuration to test a cryogenic optical system inside a vacuum chamber was introduced with the Thermal Sieve. The TS provides thermal decoupling between a cryogenic optical system under test and a collimator operating at ambient temperature, while passing the test beam wavefront without significant degradation.

The feasibility of the conceptual configuration was demonstrated in two areas. The thermal performance was analyzed based on the analytical thermal transfer model. The final results looked promising for isolating a 30K system from a 300K collimator. A three thermal plate TS will cause thermal loading less than $200\text{mW}/\text{m}^2$ for both the ambient and the cryogenic sides of the system. The optical performance was demonstrated with the wave propagation simulation results showing that the wavefront degradation due to the TS was very small (*e.g.* $<0.006\text{waves RMS}$).

This conceptual study based on the theoretical analysis and numerical simulations provides a good baseline for the further developments of this new testing configuration. However, we acknowledge that the simplified models and approximated equations in this study such as thermal transfer equations, integrated amplitude and phase error may not fully describe the real performance of TS. Also, there might be some second order effects. For instance, the primary mirror of a collimator may focus some of the thermal radiation to its secondary mirror. The actual thermal and optical performance, which will be a function of many complex factors, must be experimentally demonstrated using a proof-of-concept configuration. We are currently proposing an experimental demonstration using a sub-scale TS inside a cryogenic vacuum chamber.

Appendix

A.1 Basic functions

Because Fourier transform is frequently used in the course of analytical wave propagation in Section 3, it is convenient to define some basic functions.

Cylinder function, $cyl(r)$, which gives a circular disk in the x - y plane, is defined as below.

$$cyl(\sqrt{x^2 + y^2}) = \begin{cases} 1 & , \sqrt{x^2 + y^2} \leq 1/2 \\ 0 & , \sqrt{x^2 + y^2} > 1/2 \end{cases} \quad (23)$$

Sombbrero function, $somb(r)$, is defined using the first-order Bessel function of the first kind, J_1 .

$$somb(\sqrt{x^2 + y^2}) = \frac{2J_1(\pi \cdot \sqrt{x^2 + y^2})}{\pi \cdot \sqrt{x^2 + y^2}} \quad (24)$$

The 2D comb function, $comb(x, y)$, is defined as

$$comb(x, y) = \sum_{m=-\infty}^{\infty} \sum_{n=-\infty}^{\infty} \delta(x - m, y - n) \quad (25)$$

where $\delta(x, y)$ is the delta function.